The Astrophysical Journal, 975:227 (13pp), 2024 November 10 https://doi.org/10.3847/1538-4357/ad8153
© 2024. The Author(s). Published by the American Astronomical Society.
OPEN ACCESS

On the 3D Transport of Low-energy Galactic Cosmic-ray and Jovian Electrons in the Inner Heliosphere in the Presence of a Fisk-type Heliospheric Magnetic Field

N. E. Engelbrecht
Center for Space Research, North–West University, Potchefstroom, 2522, South Africa; n.eugene.engelbrecht@gmail.com
Received 2024 May 22; revised 2024 September 20; accepted 2024 September 28; published 2024 November 6

Abstract

Modeling the transport of low-energy (1−10 MeV) cosmic-ray electrons can lead to valuable insights as to the behavior of the heliospheric magnetic field (HMF), due to the fact that the mean free path (MFP) of these particles parallel to the HMF is significantly larger than their perpendicular MFP, and that these particles experience little in the way of drift due to gradients/curvatures in the HMF and along the heliospheric current sheet. Jovian electrons are particularly suitable for such an endeavour, as they originate from a decentral source in the inner heliosphere. To this end, the transport of these electrons is studied using a 3D, ab initio particle transport code that incorporates theoretical expressions for electron diffusion coefficients, and utilizes as inputs for these transport coefficients turbulence quantities calculated using a two-component turbulence transport model. The effects of a novel Fisk-type field on the transport of these Jovian electrons are investigated and compared with the effects of a standard Parker field.

Unified Astronomy Thesaurus concepts: Heliosphere (711); Interplanetary turbulence (830); Cosmic rays (329)

1. Introduction

Since the proposal of an alternative heliospheric magnetic field (HMF) model by L. A. Fisk (1996), as opposed to the standard E. N. Parker (1958) model, the exact nature of the large-scale HMF has been the subject of much debate. The Fisk field, and subsequent variations thereof (e.g., N. A. Schwadron 2002; N. A. Schwadron & D. J. McComas 2003; R. A. Burger & M. Hitge 2004; R. A. Burger et al. 2008; M. Hitge & R. A. Burger 2010; P. J. Steyn & R. A. Burger 2020), display considerable latitudinal meandering of field lines due to a combination of the effects of differential footpoint rotation (see, e.g., H. B. Snodgrass 1983; J. G. Beck 2000; L. Paternò 2010) and the super-radial expansion of field lines in the photosphere (see also T. H. Zurbuchen et al. 1997; L. A. Fisk et al. 1999; L. A. Fisk 2001), and would in principle allow for enhanced latitudinal particle transport relative to the Parker field (L. A. Fisk & J. R. Jokipii 1999; R. A. Burger 2005). This would then potentially provide a natural explanation for lower-than-expected galactic cosmic ray (GCR) proton differential intensities and latitude gradients, as well as high-latitude recurrent variations, observed by the Ulysses spacecraft (see, e.g., J. A. Simpson et al. 1995; B. Heber et al. 1996; M. Zhang 1997; C. Paizis et al. 1999; B. Heber 2013). However, direct observational evidence for a Fisk-type HMF has been somewhat ambiguous (see, e.g., the discussions by T. H. Zurbuchen et al. 1997; L. A. Fisk 2001; R. J. Forsyth et al. 2002; D. A. Roberts et al. 2007; R. A. Burger et al. 2008; P. J. Steyn et al. 2024), and, to date, the best evidence for the presence of such fields, albeit indirect, has come from particle transport studies.

As such, particle transport studies have confirmed the plausibility of these models by reproducing the lower-than-expected GCR proton latitude gradients (see, e.g., R. A. Burger & M. Hitge 2004; R. A. Burger et al. 2008; M. Hitge & R. A. Burger 2010), as well as the higher-latitude recurrent variations (e.g., R. A. Burger et al. 2008; N. E. Engelbrecht & R. A. Burger 2010; O. Sternal et al. 2011; J. S. Troskie et al. 2024), including the observed linear relationship between these phenomena (M. Zhang 1997). It should be noted, however, that various other mechanisms have been proposed whereby GCR latitude gradients in particular could successfully be reduced in GCR modulation models. Anisotropic perpendicular diffusion (see J. R. Jokipii et al. 1995; M. Hattingh et al. 1997a; M. S. Potgieter et al. 1997; J. Kóta & J. R. Jokipii 1998; R. A. Burger et al. 2000) has been demonstrated to reduce latitude gradients, and isotropic perpendicular diffusion, but with latitudinally varying turbulence quantities can also do so (N. E. Engelbrecht & R. A. Burger 2013a; K. D. Moloto et al. 2019; Z. Shen et al. 2021; J. S. Troskie et al. 2024), but neither of these mechanisms can reproduce the observed recurrent variations.

The Jovian magnetosphere is the main source of low-energy cosmic-ray electrons in the heliosphere (see F. B. McDonald et al. 1972; B. J. Teegarden et al. 1974; K. R. Pyle & J. A. Simpson 1977), and the transport of these particles has received considerable attention (see, e.g., D. L. Chenette et al. 1977; T. F. Conlon 1978; H. Fichtner et al. 2000; S. E. S. Ferreira et al. 2001a, 2001b; M. Zhang et al. 2007; R. D. Strauss et al. 2011; P. Dunzlaff et al. 2015; A. Vogt et al. 2020). This has been motivated, in part, by the fact that a comparison of model results between periods of good and poor magnetic connectivity between Jupiter and Earth can provide valuable insights into the transport of these particles, particularly their diffusion coefficients (e.g., M. Zhang et al. 2007; N. E. Engelbrecht et al. 2022a), as well as their residence times in the inner heliosphere (e.g., R. D. Strauss et al. 2013; A. Vogt et al. 2022). The study of Jovian electron transport could also potentially provide novel insights as to the nature of the HMF (see, e.g., R. D. Strauss et al. 2024), also due to the decentral nature of the Jovian source, and due to the fact that the transport of these particles remains relatively unaffected by

Original content from this work may be used under the terms of the Creative Commons Attribution 4.0 licence. Any further distribution of this work must maintain attribution to the author(s) and the title of the work, journal citation and DOI.

drifts, as deduced from prior modulation studies of these particles (e.g., S. E. S. Ferreira et al. 2003; S. E. S. Ferreira 2005) as well as the expected reducing influence of the higher levels of turbulence in the inner heliosphere (e.g., Z. B. Pine et al. 2020a; M. E. Cuesta et al. 2022; R. A. Burger & S. R. McKee 2023) on the drift coefficients of these low-energy, low-Larmor-radius particles (J. Minnie et al. 2007; R. C. Tautz & A. Shalchi 2012; N. E. Engelbrecht et al. 2017). Furthermore, given that the low-energy electron mean free path (MFP) parallel to the mean HMF is considerably larger than the perpendicular MFP (see, e.g., J. W. Bieber et al. 1994; M. S. Potgieter 1996; N. E. Engelbrecht et al. 2022a, 2022b), these particles would in principle be extremely sensitive to latitudinal excursions of HMF lines. This idea has been explored before to some extent, by N. E. Engelbrecht & R. A. Burger (2010) and O. Sternal et al. (2011), where the influence of a Fisk–Parker hybrid field on low-energy cosmic-ray electron latitude gradients and relative amplitudes was investigated. Those studies, however, had several limitations. First, the Fisk-type field they employed assumed a constant solar wind speed (see, e.g., R. A. Burger & M. Hitge 2004; P. J. Steyn & R. A. Burger 2020), which is not accurate for solar minimum conditions (e.g., D. J. McComas et al. 2000, 2003). Second, those studies employed simple radial power-law expressions to model the spatial dependences of turbulence quantities essential to the calculation of electron diffusion coefficients such as magnetic variances and correlation lengths, assuming no latitudinal dependence for these quantities. This, too, is not in agreement with observations (see, e.g., R. J. Forsyth et al. 1996; B. Bavassano et al. 2000a, 2000a; G. Erdős & A. Balogh 2005). Lastly, these studies employ for the dissipation range onset wavenumber, a parameter that N. E. Engelbrecht & R. A. Burger (2010) demonstrate to significantly influence computed GCR electron intensities, simple extrapolations of fits to 1 au observations of this quantity reported by R. J. Leamon et al. (2000). It is unclear whether such an approach would be valid throughout the heliosphere, and as such a more self-consistent approach to estimating this quantity, such as that proposed by N. E. Engelbrecht & R. D. Strauss (2018; more on which below), would perhaps be better suited to such transport studies. In brief, electron transport is known to be extremely sensitive to assumptions made as to diffusion coefficients, and hence the turbulence quantities these coefficients depend upon (e.g., N. E. Engelbrecht & R. A. Burger 2010, 2013b; N. E. Engelbrecht 2019), and therefore these quantities require careful modeling in as self-consistent a manner as is possible.

The present study aims to do this in order to elucidate the effects a Schwadron–Parker HMF, which is derived assuming a latitude-dependent solar wind speed (see N. A. Schwadron 2002; N. A. Schwadron & D. J. McComas 2003; M. Hitge & R. A. Burger 2010), could have on low-energy (1−10 MeV) cosmic-ray electrons of both Jovian and galactic origin, the energy range being chosen precisely where Jovian electrons are expected from observational and modulation studies to form the predominant component of these particles (e.g., D. L. Chenette et al. 1977; D. Moses 1987; S. E. S. Ferreira et al. 2001a). To this end, turbulence quantities entering into electron transport coefficients are carefully modeled using a two-component turbulence transport model (TTM) proposed by S. Oughton et al. (2011) that yields results in reasonable to good agreement with spacecraft observations both within and beyond the heliospheric ecliptic plane (see, e.g., N. E. Engelbrecht & R. A. Burger 2013a; N. E. Engelbrecht & R. D. Strauss 2018). Although more recent models exist that have also been been shown to yield results in good agreement with observations (see, e.g., G. P. Zank et al. 2012, 2017; A. V. Usmanov et al. 2016; T. Wiengarten et al. 2016; A. V. Usmanov et al. 2018; L. Adhikari et al. 2021a; N. E. Engelbrecht et al. 2022b), the present model is used as it has been successfully employed in previous cosmic-ray modulation studies, particularly those of GCR electrons (see N. E. Engelbrecht & R. A. Burger 2013b; N. E. Engelbrecht 2019). Such a study, modeling Jovian electron transport from first principles by using turbulence quantities yielded by a TTM, has not before been embarked upon, and as such the aim of the present study is not to painstakingly fit existing data, but rather to investigate the effects such a HMF would have on electron intensities, latitude gradients, and relative amplitudes computed in a physics-first manner in order to ascertain whether evidence for such a HMF could be gleaned from observations of the same. That being said, at present few analyses of such observations exist, particularly at higher latitudes (see, e.g., B. Heber et al. 2008; O. Sternal et al. 2011; P. Kühl et al. 2013), and the present study aims to provide motivation for future analyses as well as theoretical results with which they can be compared. This is particularly relevant given the large amount of low-energy electron measurements from prior missions (see R. D. Strauss et al. 2024), as well as expected observations from existing missions, such as data from the off-ecliptic phase of the Solar Orbiter trajectory (see D. Müller et al. 2020), and upcoming missions such as the Jupiter Icy Moons Explorer (see O. Grasset et al. 2013; J. Rodríguez-Pacheco et al. 2020).

This study is organized as follows. The next section (Section 2) outlines the modulation model employed, detailing assumptions as to the large- and small-scale plasma quantities modeled here (Section 2.1). This includes a discussion of the TTM solved (Section 2.2), and the diffusion coefficients implemented (Section 2.3), in the modulation code. Subsequently, results as to GCR and Jovian electron differential intensities, latitude gradients, and relative amplitudes are discussed (Section 3). the study closes with a section devoted to a summary of said results, and the conclusions to be drawn therefrom (Section 4).

2. The Transport Model

We model the transport of Jovian and galactic electrons, using the 3D, steady-state modulation code of R. A. Burger & M. Hattingh (1995) and M. Hattingh et al. (1997), as refined by N. E. Engelbrecht & R. A. Burger (2013a, 2013b), to solve the E. N. Parker (1965) cosmic-ray transport equation using an alternating-direction implicit numerical scheme (see D. W. Peaceman & H. H. Rachford 1955) as opposed to more commonly used stochastic techniques (e.g., R. D. Strauss & F. Effenberger 2017), which for this application are considerably more computationally expensive. The Parker transport equation, given by

$$\frac{\partial f}{\partial t} = \nabla \cdot (\boldsymbol{K} \cdot \nabla f) - \boldsymbol{V}_{\rm sw} \cdot \nabla f + \frac{1}{3}(\nabla \cdot V_{\rm sw}) \frac{\partial f}{\partial \ln p} + Q, \quad (1)$$

with $f(\boldsymbol{r}, p, t) = p^{-2} j_T$ the omnidirectional cosmic-ray distribution function (H. Moraal 2013), describes the diffusion (and drift) of GCRs via the diffusion tensor $\boldsymbol{K}$, the convection of these particles with the solar wind, and their adiabatic energy changes, with Q some heliospheric source of cosmic rays, in

this case the Jovian magnetosphere. This is done for both GCR electrons and Jovian electrons, the latter being incorporated into the code in precisely the same manner as discussed by S. E. S. Ferreira et al. (2001a, 2001b). As a Jovian source spectrum, used to model Q, the expression proposed by A. Vogt et al. (2018),

$$j_{\rm jov}(E) = 1.029 \cdot 10^4 (E/E_0)^{-1.63} e^{-E/E_b}, \quad (2)$$

with $E_b = 9.4$ MeV, is employed. Where galactic electron transport is concerned, an input spectrum location is assumed at 84 au, the nominal location of the termination shock as observed by Voyager 2 (see H. Li et al. 2008; J. R. Jokipii 2013; D. J. McComas et al. 2019; J. D. Richardson et al. 2022, and references therein). Note, however, that no termination shock is included in this model. The observationally motivated boundary spectrum proposed by N. E. Engelbrecht (2019) is employed, and is given as a function of rigidity P by

$$j_B = \frac{0.225 P^{-2.75}}{1.0 + 0.95 P^{-2.52}} + 1.75 \times 10^{-6} P^{-3.0}, \quad (3)$$

and is constructed at lower energies from Voyager observations near the termination shock reported by W. R. Webber et al. (2017), and at higher energies from PAMELA observations reported by O. Adriani et al. (2011). Note that both input spectra used here are in units of units of particles $\rm m^{-2}\,s^{-1}\,sr^{-1}\,MeV^{-1}$. The radial distance for the input spectrum is chosen to be such due to the fact that the turbulence model employed here is strictly only valid within the termination shock, due in part to it only modeling the transport of transverse turbulent quantities. This limitation is partly due to the fact that turbulence in the heliosheath is observed to be predominantly compressive in nature (see, e.g., L. F. Burlaga & N. F. Ness 2012; L. F. Burlaga et al. 2014; H. Fichtner et al. 2020; F. Fraternale et al. 2022). An input spectrum constructed from in situ observations at 95 au can at least ameliorate any potential overestimation of GCR electron differential intensities, resulting from the modulation of these particles in the heliosheath (known to be considerable for GCR protons, e.g., E. C. Stone et al. 2013), that would arise from placing a full local interstellar spectrum at this radial distance. Latitude gradients are here calculated following R. A. Burger et al. (2008) and M. Hitge & R. A. Burger (2010), for example, such that

$$G_\theta(r) = \frac{1}{\theta_1 - \theta_2} \ln\left[\frac{j_T(r, \theta_2)}{j_T(r, \theta_1)}\right] \times 100\%, \quad (4)$$

with $\theta_1 = 90^\circ$ and $\theta_2 = 10^\circ$ colatitude, and at a radial distance of 2 au. Relative amplitudes are calculated following M. Zhang (1997) and M. Hitge & R. A. Burger (2010) such that

$$\Delta j_T(r, \theta, \phi, P) = \frac{j_T^{\max}(r, \theta, \phi, P) - j_T^{\min}(r, \theta, \phi, P)}{\langle j_T(r, \theta, \phi, P)\rangle_\phi} \times 100\%, \quad (5)$$

and are evaluated at a colatitude of 50° (where the Schwadron–Parker field is expected to be very Fisk-like) and at 2 au. As the focus here is on the study of the transport of low-energy electrons, the present study will only consider a range of energies extending from $E = 1-10$ MeV, as this is the range of energies over which the Jovian electron source is expected to predominate in the inner heliosphere (see, e.g., S. E. S. Ferreira et al. 2001a; R. D. Strauss et al. 2013, 2024; R. R. Nndanganeni & M. S. Potgieter 2018; A. Vogt et al. 2018, 2020).

2.1. Large-scale Plasma Quantities

The Parker transport equation is here solved assuming either a purely E. N. Parker (1958) field, or a Schwadron–Parker hybrid field as proposed by M. Hitge & R. A. Burger (2010; see also N. A. Schwadron 2002; P. J. Steyn & R. A. Burger 2020), which is given by

$$\begin{aligned} B_r &= \frac{A}{r^2}\left(1 + \frac{r}{V_{\rm sw}^2}\omega^* \sin\beta^* \sin\phi^* \frac{dV_{\rm sw}}{d\theta}\right) \\ B_\theta &= \frac{A}{rV_{\rm sw}}\omega^* \sin\beta^* \sin\phi^* \\ B_\phi &= \frac{A}{rV_{\rm sw}}[\omega^* \cos\beta^* \sin\theta \\ &\quad + \frac{d}{d\theta}(\omega^* \sin\beta^* \sin\theta)\cos\phi^* - \Omega \sin\theta\Big], \end{aligned} \quad (6)$$

where $\phi^* = \phi + \Omega r/V_{\rm sw} - \phi_0$ and ϕ_0 are constant. Furthermore, $\omega^* = \omega/4F_s$, with ω the differential rotation rate of the HMF footpoints, here assumed to be constant and equal to $\Omega/4$; $\beta^* = \beta F_s$ is a parameter that governs the nonradial expansion of magnetic field lines in the region between the photosphere and source surface (see R. A. Burger & M. Hitge 2004; R. A. Burger et al. 2008; P. J. Steyn & R. A. Burger 2020, for more detail); and F_s is a latitude-dependent transition function defined so that the above field is a pure Schwadron field should $F_s = 1$ and a pure Parker field should $F_s = 0$, and is given by (R. A. Burger et al. 2008)

$$F_S = \begin{cases} \{\tanh[\delta_p\theta] + \tanh[\delta_p(\theta - \pi)] - \tanh[\delta_e(\theta - \theta'_b)]\}^4 & \text{if } \theta \in [0, \theta'_b); \\ 0 & \text{if } \theta \in [\theta'_b, \pi - \theta'_b]; \\ \{\tanh[\delta_p\theta] + \tanh[\delta_p(\theta - \pi)] - \tanh[\delta_e(\theta - \pi - \theta'_b)]\}^4 & \text{if } \theta \in (\pi - \theta'_b, \pi]. \end{cases} \quad (7)$$

Here $\delta_p = 5.0 = \delta_e$ are constants affecting the gradients of F_S, their values being chosen so as to coincide with those of R. A. Burger et al. (2008) and O. Sternal et al. (2011), and $\theta'_b = 80/180\pi$. Note that Equation (6) is divergence free, due to F_s being solely a function of colatitude θ (see M. Hitge & R. A. Burger 2010; P. J. Steyn & R. A. Burger 2020, for more detail). The latitudinal solar wind speed profile during solar minimum is modeled using

$$V_{\rm sw}(\theta) = 400 \text{ km s}^{-1}\begin{cases}1.5 - 0.5\tanh\left[8(\theta - \pi/2 + \alpha + \delta_t)\right] & \text{if}\theta \leqslant \pi/2;\\ 1.5 + 0.5\tanh\left[8(\theta - \pi/2 - \alpha - \delta_t)\right] & \text{if}\theta > \pi/2\end{cases}, \quad (8)$$

with α the tilt angle of the heliospheric current sheet (assumed here to take a solar minimum value of 10°), θ the colatitude, and $\delta_t = 20\pi/180$ radians. Note that the factor of 8 governs the steepness of the latitudinal transition of the function.

2.2. Turbulence

The two-component TTM of S. Oughton et al. (2011), as solved by N. E. Engelbrecht & R. D. Strauss (2018), is employed here to model the turbulence quantities required as inputs for the diffusion coefficients used in this study (discussed below) throughout the heliosphere. Note that the present study only takes into account solar minimum conditions, and therefore does not attempt to model the observed solar cycle dependences of various turbulence quantities (L. L. Zhao et al. 2018; N. E. Engelbrecht & C. P. Wolmarans 2020; R. A. Burger et al. 2022). This is done in order to calculate estimates of the dissipation range onset wavenumber as outlined in that study, to which computed low-energy electron intensities are known to display significant sensitivities (N. E. Engelbrecht & R. A. Burger 2010). The TTM is given by

$$\frac{dZ^2}{dr} = -[1 + M\sigma_D - C_{\rm sh}^Z]\frac{Z^2}{r} - \frac{\alpha f}{V_{\rm sw}}\frac{Z^3}{l} - \frac{2\alpha f_{ZW}^+}{V_{\rm sw}}\frac{WZ^2}{l}\frac{1}{1 + Z/W} + \frac{2\alpha X^+}{V_{\rm sw}}$$

$$\frac{dW^2}{dr} = -[1 + M\tilde{\sigma}_D - C_{\rm sh}^W]\frac{W^2}{r} - \frac{\tilde{\alpha}\tilde{f}}{V_{\rm sw}}\frac{ZW^2}{\lambda}\frac{2}{1 + \lambda/l} - \frac{2\tilde{\alpha}(1 - \tilde{\sigma}_c^2)}{V_{\rm sw}}\frac{W^4\lambda_{c,s}}{\lambda^2 V_{\rm A}} - \frac{2\alpha X^+}{V_{\rm sw}} + \frac{\dot{E}_{PI}}{V_{\rm sw}}$$

$$\frac{dl}{dr} = -\hat{C}_{\rm sh}^Z\frac{l}{r} + \frac{\beta}{V_{\rm sw}}\left[fZ + f_{ZW}^+\frac{2W}{1 + Z/W} - \frac{2lX^+}{Z^2}\right]$$

$$\frac{d\lambda}{dr} = -\hat{C}_{\rm sh}^W\frac{\lambda}{r} + \frac{2\tilde{\beta}}{V_{\rm sw}}\left[\frac{\tilde{f}Z}{1 + \lambda/l} + (1 - \tilde{\sigma}_c^2)\frac{W^2\lambda_{c,s}}{\lambda V_{\rm A}} + \frac{\alpha\lambda X^+}{\tilde{\alpha}W^2}\right]$$

$$\frac{d\lambda_{c,s}}{dr} = -\hat{C}_{\rm sh}^W\frac{\lambda_{c,s}}{r} + 2\tilde{\alpha}(1 - \tilde{\sigma}_c^2)\frac{W^2\lambda_{c,s}^2}{V_{\rm sw}V_{\rm A}\lambda^2} - (\lambda_{c,s} - \lambda_{\rm res})\frac{\dot{E}_{PI}}{V_{\rm sw}W^2}$$

$$\frac{d\sigma_c}{dr} = \frac{\alpha}{V_{\rm sw}}\left[\frac{f'Z}{l} + \frac{f_{ZW}{}'W}{l}\frac{2}{1 + Z/W} - \frac{2(\sigma_c X^+ - X^-)}{Z^2}\right] - \left[\frac{C_{\rm sh}^Z - M\sigma_D}{r}\right]\sigma_c$$

$$\frac{d\tilde{\sigma}_c}{dr} = \frac{2\tilde{\alpha}}{V_{\rm sw}}\left[\frac{\tilde{f}'}{1 + \lambda/l}\frac{Z}{\lambda} + \tilde{\sigma}_c(1 - \tilde{\sigma}_c^2)\frac{W^2\lambda_{c,s}}{\lambda^2 V_{\rm A}}\right] + \frac{2\alpha(\tilde{\sigma}_c X^+ - X^-)}{V_{\rm sw}W^2} - \left[\frac{C_{\rm sh}^W - M\tilde{\sigma}_D}{r} + \frac{\dot{E}_{PI}}{V_{\rm sw}W^2}\right]\tilde{\sigma}_c$$

$$\frac{dT_p}{dr} = -\frac{4}{3}\frac{T_p}{r} + f_p\left[\frac{\alpha m_p}{3V_s k_B}\left(\frac{fZ^3}{l} + \frac{2f_{ZW}^+}{1 + Z/W}\frac{WZ^2}{l}\right) + \frac{2\tilde{\alpha}m_p}{3V_s k_B}\frac{\tilde{f}}{1 + \lambda/l}\frac{ZW^2}{\lambda} + \frac{2\tilde{\alpha}m_p}{3V_s k_B}(1 - \tilde{\sigma}_c^2)\frac{W^4\lambda_{c,s}}{\lambda^2 V_{\rm A}}\right] + \frac{T_e - T_p}{\tau_c V_s}$$

$$\frac{dT_e}{dr} = -\frac{4}{3}\frac{T_e}{r} + (1 - f_p)\left[\frac{\alpha m_p}{3V_s k_B}\left(\frac{fZ^3}{l} + \frac{2f_{ZW}^+}{1 + Z/W}\frac{WZ^2}{l}\right) + \frac{2\tilde{\alpha}m_p}{3V_s k_B}\frac{\tilde{f}}{1 + \lambda/l}\frac{ZW^2}{\lambda} + \frac{2\tilde{\alpha}m_p}{3V_s k_B}(1 - \tilde{\sigma}_c^2)\frac{W^4\lambda_{c,s}}{\lambda^2 V_{\rm A}}\right] - \frac{T_e - T_p}{\tau_c V_s} - \frac{2}{3V_s k_B n_p}\nabla\cdot\vec{q}_e.$$

In this model, (half) the total turbulent fluctuation energies are denoted respectively by W^2 and Z^2 (see also S. Oughton et al. 2006), with corresponding perpendicular correlation scales denoted by l and λ, with parallel correlation scale $\lambda_{c,s}$. The quasi-2D normalized cross-helicity is denoted by σ_c, with a tilde indicating its wave-like counterpart. These quantities do not enter into the calculations of diffusion coefficients in the model, but are still solved for, for self-consistency. The variable $V_{\rm A}$ indicates the global Alfvén speed. The quantities X^+ and X^- denote nonlinear interaction terms, which are discussed in more detail in N. E. Engelbrecht & R. D. Strauss (2018). To solve the above, an 84 au heliosphere is assumed for consistency with the modulation code, and a solar wind profile given by Equation (8) is used, to mimic solar minimum conditions, employing a 4th-order Runge–Kutta solver with boundary values set as outlined by N. E. Engelbrecht & R. A. Burger (2013a) and N. E. Engelbrecht & R. D. Strauss (2018), and listed in Table 1. Although this TTM is 1D, it is solved here along radial spokes of constant colatitude and azimuth, following the approach discussed by N. E. Engelbrecht & R. A. Burger (2013a), in order to provide a 3D array of turbulence quantities that can then be used as inputs for the modulation code in order to calculate electron diffusion coefficients. As such, large-scale input parameters for the TTM are modeled according to the particular colatitude and azimuth for each particular spoke. For example, radial spokes corresponding to polar colatitudes have higher solar wind speeds associated with them, calculated according to Equation (8). Accordingly, boundary values at 0.3 au are also scaled with colatitude, using hyperbolic tangent functions with the same properties as Equation (8), as discussed by N. E. Engelbrecht & R. A. Burger (2013a). Boundary values in the ecliptic, versus those over the poles, are given in Table 1. Polar boundary conditions are difficult to ascertain, as there are less out-of-ecliptic observations to motivate their choice. As such, those in the present study are chosen so as to achieve as much agreement as possible with polar Ulysses observations (e.g., R. J. Forsyth et al. 1996; B. Bavassano et al. 2000a, 2000b; T. S. Horbury & A. Balogh 2001; G. Erdős & A. Balogh 2005), as well as with turbulence observations reported from analyses of data intervals

Table 1
Boundary Values Assumed at 0.3 au for the Two-component TTM

Quantity	Units	Ecliptic Values	Polar Values
Z^2	$km^2\ s^{-2}$	1250	1600
W^2	$km^2\ s^{-2}$	350	2000
λ	au	0.004	0.015
l	au	0.004	0.015
$\lambda_{c,s}$	au	0.011	0.011
σ_c	…	0.6	0.8
$\tilde{\sigma}_c$	…	0.6	0.8
T_p	K	4×10^5	2×10^6
T_e	K	7×10^5	7×10^5

corresponding to fast solar wind conditions at 1 au (e.g., S. Dasso et al. 2005; J. M. Weygand et al. 2011), which behave similarly to Ulysses observations in the fast solar wind during solar minimum (B. Bavassano et al. 2000a). Over the poles, boundary values were chosen to reflect larger fluctuations reported in these regions (e.g., R. J. Forsyth et al. 1996) as well as a wave-like fluctuation-dominated anisotropy, as reported by S. Dasso et al. (2005) and J. M. Weygand et al. (2011), for example, for fast streams in the ecliptic, although it is not exactly clear what this anisotropy would be. Therefore, boundary values were chosen to reflect the ratios of wave-like to quasi-2D correlation scales reported in those studies. Emphasis, however, was placed on finding agreement with the larger (relative to the ecliptic) Ulysses values for the correlation scale. The stream-shear term $C_{\rm sh}$ is also modeled in a colatitude-dependent fashion, in the manner described by B. Breech et al. (2008; see also N. E. Engelbrecht & R. A. Burger 2013a), thereby taking into account the enhancement of stream-shear effects expected at, for example, the transition region between the slow and fast solar wind at intermediate latitudes. It should be noted that this shear term is similar to that introduced by G. P. Zank et al. (1996), and that it has been argued by G. P. Zank et al. (2017) that the turbulent shear source introduced by G. P. Zank et al. (1996) is like an amplification term, rather than a pure source term.

Pickup-ion-related effects, included via the approach taken by S. Oughton et al. (2011), are neglected in the calculation of magnetic variances and correlation scales entering into the modulation code (see, e.g., N. E. Engelbrecht 2017, and discussion therein) but not in the calculation of temperatures, and therefore by implication dissipation range onset wavenumbers (discussed below), necessitating the separate solution of the above equations with the pickup ion source term on and off. The mixing term is taken as $M = \cos^2\psi$, with ψ the HMF winding angle. The de Kármán–Taylor constants are chosen so that $\alpha = 2\beta = 0.125$ (S. Oughton et al. 2011) following C. Pei et al. (2010), and a normalized energy difference $\sigma_D = -1/3$ is assumed, implying an assumed Alfvén ratio of 0.5 (e.g., D. A. Roberts et al. 1987). It should be noted, however, that σ_D has been shown, both observationally and theoretically (see, e.g., L. Adhikari et al. 2017, 2021b), to vary considerably with radial distance. In the temperature equations, the assumption is here made that proton heat conduction is negligible relative to electron heat conduction (see B. Breech et al. 2009), which is modeled with the term $\nabla \cdot \boldsymbol{q}_e$. This, in turn, is modeled using a parametric fit by S. R. Cranmer et al. (2009) to Helios and Ulysses spacecraft observations (reported by E. Marsch et al. 1982; W. G. Pilipp et al. 1990; E. E. Scime et al. 1994), so that

$$\ln\left(\frac{q_{\parallel,e}}{q_o}\right) = -0.7032 - 2.115x - 0.2545x^2, \tag{9}$$

with $q_o = 0.01\ \mathrm{erg\ cm^2\ s^{-1}}$ and $x = \ln(r/1\mathrm{au})$. In the present study, following those of B. Breech et al. (2009) and N. E. Engelbrecht & R. D. Strauss (2018), it is assumed that the electron heat flux is latitude independent, motivated by the analysis of Ulysses observations by E. E. Scime (1999), who report an essentially constant electron heat flux from heliographic latitudes of $-80°$ to $+80°$. Furthermore, E. E. Scime et al. (2001) confirm this result, and report from a further analysis of Ulysses observations that no correlation can be found between solar wind speed and electron heat flux, regardless of solar activity level. It should be noted, however, that J. S. Halekas et al. (2021) report, from an analysis of Parker Solar Probe observations at distances of 0.125−0.25 au, that the observed electron heat flux is anticorrelated with solar wind speed (see also J. S. Halekas et al. 2020). It is unclear whether the differences between what was reported for Ulysses observations versus Parker Solar Probe observations is a result of the different radial distances at which the analyzed observations were taken, given that C. Salem et al. (2003) report no such anticorrelation in their analyses of 1 au Wind data. However, such differences, when taken into account, can influence the outputs yielded by the TTM, and will be the subject of future investigation. Coulomb interactions between the two species, although demonstrated to be negligible by N. E. Engelbrecht & R. D. Strauss (2018), are here taken into account, and are modeled after S. R. Cranmer et al. (2009) using the term $(T_e - T_p)/\tau_c V_s$, with τ_c a Coulomb collision term. For more detail as to the solution of this model, as specifically pertaining to electron temperatures, see N. E. Engelbrecht & R. A. Burger (2013a) and N. E. Engelbrecht & R. D. Strauss (2018). The influence of the Schwadron–Parker hybrid field on the solution of the above TTM has been demonstrated by N. Engelbrecht (2012) to be negligible, even in the inner heliosphere. This is due to the fact that the Parker and Schwadron–Parker hybrid fields do not differ greatly in magnitude, and that the mixing term M, dependent as it is on the HMF winding angle, does not play a significant role in the solutions to the TTM relative to other terms, such as the stream-shear term. Therefore, in the solution of this model a purely Parker field is employed. To find the onset wavenumber of the slab dissipation range, the smallest value of k where the Doppler-shifted cyclotron resonance between dispersive waves and thermal particles occurs is found (N. E. Engelbrecht & R. D. Strauss 2018). Thus, dissipation range onset wavenumbers are calculated using the proton temperature with

$$k_d \approx \frac{\Omega_p}{V_{\rm A} + 3v_{\rm th}^p}, \tag{10}$$

with $v_{\rm th}^p$ the proton thermal speed. Calculating the proton temperature required for this calculation necessitates the calculation of the electron temperature also, as the turbulent energy goes to heat both protons and electrons. The question naturally arises as to how much of this energy goes to heating

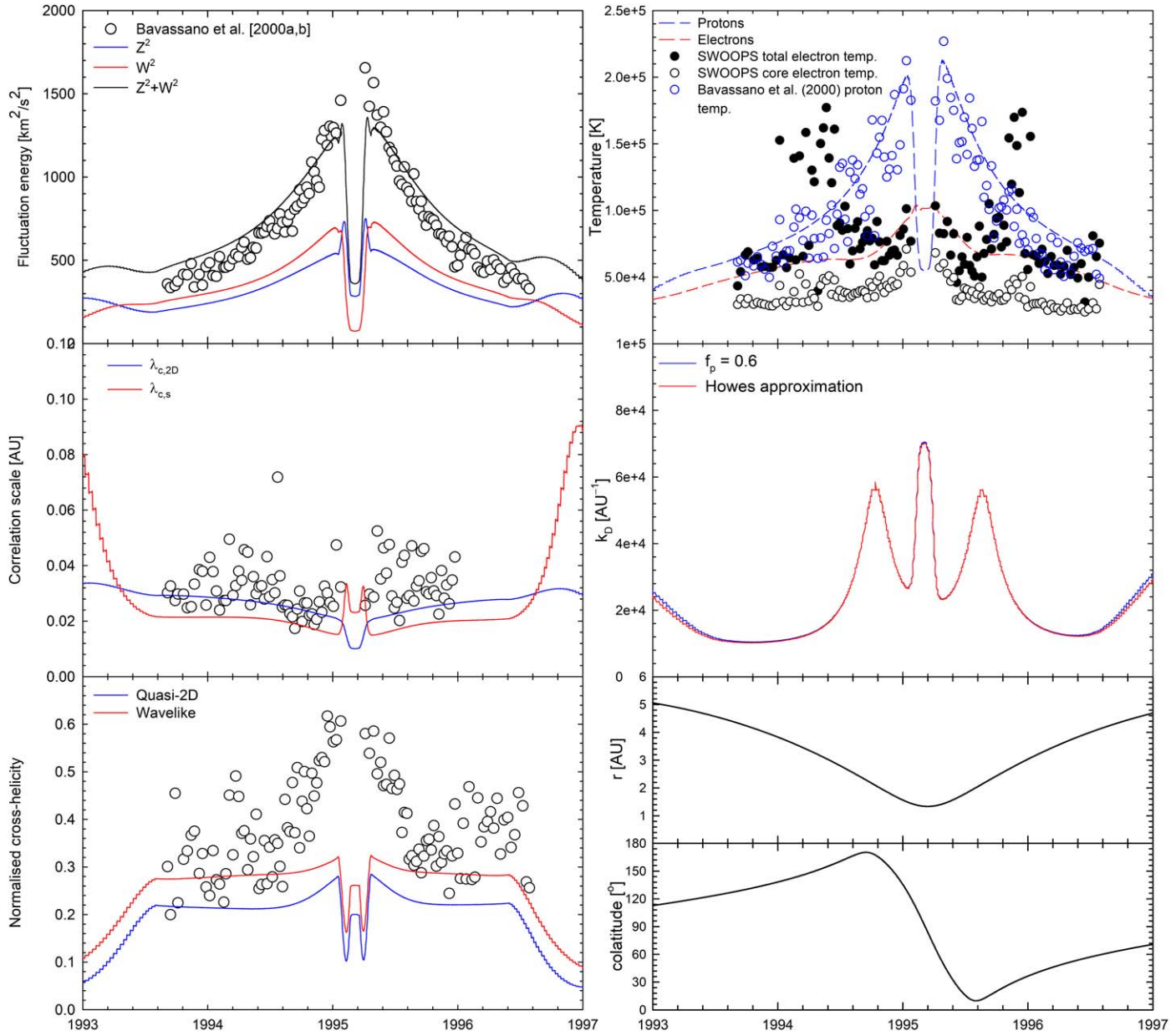


Figure 1. Left panels, top to bottom: fluctuation energies, correlation scales, and normalized cross-helicities yielded by the S. Oughton et al. (2011) TTM along the trajectory of the Ulysses spacecraft, alongside observations of the same reported by B. Bavassano et al. (2000a, 2000b). Right panels, top to bottom: electron and proton temperatures, and resulting dissipation range onset wavenumbers, calculated from the TTM along Ulysses' trajectory, alongside appropriate SWOOPs and B. Bavassano et al. (2000a, 2000b) observations. Bottom-right panels indicate the radial and colatitudinal positions of the Ulysses spacecraft, to guide the eye. Figure adapted from N. E. Engelbrecht & R. D. Strauss (2018). Note that the times given in the *x*-axes of the plots containing quantities calculated with the TTM serve only to indicate that those values correspond to the position of the spacecraft at that particular time, which can then be read off the bottom-right panels.

the protons. To that end, the present study models this fraction $f_p \in [0,\ 1]$ in two ways. The first is to assume a constant $f_p = 0.6$, following such approaches as S. R. Cranmer et al. (2009), B. Breech et al. (2009), and L. Adhikari et al. (2021b), although this has been shown to possibly be an underestimate in the very inner heliosphere (see, e.g., R. Bandyopadhyay et al. 2023; L. Adhikari et al. 2024). A second approach would be to assume a radial dependence for this quantity. To this end, the present study employs the parametric fit proposed by N. E. Engelbrecht & R. D. Strauss (2018) to an analytical result for f_p due to a turbulent cascade in a fully ionized, weakly collisional plasma derived by G. G. Howes (2010), and given by

$$f_p = \begin{cases} 0.6, & r \leqslant 1 \text{ au}; \\ 1.367 \exp\left[-1/(3.2r^{2.2})\right] - 0.4, & r > 1 \text{ au}. \end{cases} \tag{11}$$

A possible latitudinal dependence for this quantity is not incorporated here, as S. R. Cranmer et al. (2009) report only a weak latitudinal dependence for f_p.

Figure 1 displays the behavior of the turbulence quantities yielded by the S. Oughton et al. (2011) TTM along the trajectory of the Ulysses spacecraft during the first fast latitude scan (see K. P. Wenzel et al. 1992; K.-P. Wenzel 1995, for more details), along with spacecraft observations appropriate to

each particular quantity (B. Bavassano et al. 2000a, 2000b), as well as the radial and meridional positions of this spacecraft (bottom-right panel). Note that the times given in the x-axes of the plots containing quantities calculated with the TTM serve only to indicate that those values correspond to the position of the spacecraft at that particular time, which can then be read off the bottom-right panels of the figure. While the fluctuation energies Z^2 and W^2 are in reasonably good agreement with observations, displaying a increase toward higher latitudes and decreasing with radial distances, the agreement of the computed correlation scales is less good. It should be noted, however, that the correlation scale observations display a significant scatter, possibly due to the influence of the resolution of the data analyzed on the resulting correlation scales, as well as effects arising from the fact that data from a single spacecraft are being analyzed (see, e.g., W. H. Matthaeus et al. 2005; K. T. Osman & T. S. Horbury 2007; T. S. Horbury & K. T. Osman 2008; J. J. Isaacs et al. 2015). Computed normalized cross-helicities are in poor agreement with observations. This may be due to the fact that the present model assumes an overly large value for the normalized energy difference at these colatitudes, and would need to be revisited with a model not constrained to a constant value of σ_D (see, e.g., L. Adhikari et al. 2022). However, this does not influence the results of this study as pertaining to particle transport, as normalized cross-helicities are not taken into account in the calculation of transport coefficients entering into the modulation code. It should be noted that A. V. Usmanov et al. (2018) report, using a single-component TTM coupled to a magnetohydrodynamic code, an inverse correlation between turbulence energy and correlation length, and higher normalized cross-helicity at high latitudes than at low latitudes. The top-right panel of Figure 1 shows the computed proton and electron temperatures, alongside Ulysses proton temperatures and SWOOPS (see S. J. Bame et al. 1992) measurements of the core and total electron temperatures. Note that only results calculated using Equation(11) are shown, as they are nearly identical to those calculated assuming a constant $f_p = 0.6$ at these radial distances. For protons, model results are in reasonable agreement with observations, as they are for electrons, excepting at intermediate latitudes. The panel below this shows the corresponding dissipation range onset wavenumbers, calculated for both approaches to f_p employed here, using Equation (10). This quantity displays considerable radial and meridional variation, with larger values in the ecliptic plane than over the poles, and a steady drop with increasing radial distance. The choice of f_p at these radial distances does not greatly influence this quantity, although it would play a greater role at larger distances (N. E. Engelbrecht & R. D. Strauss 2018). Therefore, as the emphasis of the present study lies on the modulation of Jovian electrons, only Equation (11) will be employed in the calculation of particle transport coefficients in the modulation code. For more detail as to the spatial evolution of the turbulence quantities yielded by the S. Oughton et al. (2011) TTM under various assumptions, see N. E. Engelbrecht & R. A. Burger (2013a, 2015) and N. E. Engelbrecht & R. D. Strauss (2018).

2.3. Diffusion Coefficients

The turbulence quantities discussed above are used as inputs for a quasi-linear theory (J. R. Jokipii 1966) parallel MFP derived assuming a dissipation range and the damping model of dynamical turbulence (see A. Teufel & R. Schlickeiser 2003; N. E. Engelbrecht & R. A. Burger 2013b), a choice motivated by the fact that this expression yields electron MFPs closest to those expected for Jovians (e.g., N. E. Engelbrecht et al. 2022a; A. Vogt et al. 2022), and given by

$$\lambda_{\parallel} = \frac{3s}{\sqrt{\pi}(s-1)}\frac{R^2}{k_m}\frac{B_0^2}{\delta B_s^2}\left[\frac{1}{4\sqrt{\pi}} + {}_2F_1\left(1, \frac{1}{p-1}, \frac{p}{p-1}; -\frac{\pi a}{f}Q^{p-2}\right)\frac{\sqrt{\pi}a}{fR^sQ^{p-s}} + \frac{2R^s}{\sqrt{\pi}(2-s)(4-s)}\right], \tag{12}$$

where δB_s^2 denotes the slab variance (computed from W^2; see N. E. Engelbrecht & R. A. Burger 2013a), and $-s$ and $-p$ the inertial and dissipation range spectral indices, chosen here to be equal to the Kolmogorov value in the case of the former (see, e.g., C. W. Smith et al. 2006; Z. B. Pine et al. 2020b; R. A. Burger et al. 2022; X. Zhu et al. 2024) and an observationally motivated value of -2.6 for the latter (C. W. Smith et al. 2006). Both these quantities have been demonstrated to vary considerably in the very inner ($r < 1$ au) heliosphere (e.g., C. H. K. Chen et al. 2020; L. L. Zhao et al. 2020; N. Davis et al. 2023; S. Lotz et al. 2023), but this variation is not taken into account here, as the particles in question are expected to spend more time beyond this radial distance. Furthermore, $R = R_L k_m = R_L/\lambda_s$, with R_L the maximal electron Larmor radius, and $Q = R_L k_d$. Lastly, $f = 2(p-s)/\pi(p-2)(2-s)$, and $a = v/\alpha_D V_A$, with v the particle speed, and $\alpha_D \in [0, 1]$ a parameter governing dynamical effects (see, e.g., J. W. Bieber et al. 1994), set to a value of unity here. A nonlinear guiding center (W. H. Matthaeus et al. 2003) perpendicular MFP (see A. Shalchi et al. 2004; R. A. Burger et al. 2008) is employed here, where

$$\lambda_{\perp} = \left[\alpha^2\sqrt{3\pi}\frac{2\nu-1}{\nu}\frac{\Gamma(\nu)}{\Gamma(\nu-1/2)}\lambda_{2D}\frac{\delta B_{2D}^2}{B_0^2}\right]^{2/3}\lambda_{\parallel}^{1/3}, \tag{13}$$

with ν denoting half the Kolmogorov inertial range spectral index, and motivated by the relative tractability of this expression relative to others derived from more recent scattering theories (for examples of which, see N. E. Engelbrecht et al. 2022b), as well as by the fact that the use of this expression in prior modulation studies has led to computed GCR proton and antiproton intensities in reasonable to good agreement with spacecraft observations (e.g., K. D. Moloto et al. 2018; N. Engelbrecht & K. D. Moloto 2021). Dynamical effects on the perpendicular MFP are neglected here, as these have been demonstrated to be negligible (N. Dempers & N. E. Engelbrecht 2020), and α a parameter taken to equal $1/\sqrt{3}$, following the simulation results of W. H. Matthaeus et al. (2003). Drift effects are switched off, as these have been shown to be insignificant for electrons at the energies considered here (e.g., M. S. Potgieter 1996; S. E. S. Ferreira et al. 2001a, 2001b). Figure 2 shows the parallel and perpendicular MFPs discussed above, calculated at an energy of 6 MeV along the trajectory of Ulysses during its first fast latitude scan using inputs from the TTM shown in Figure 1,

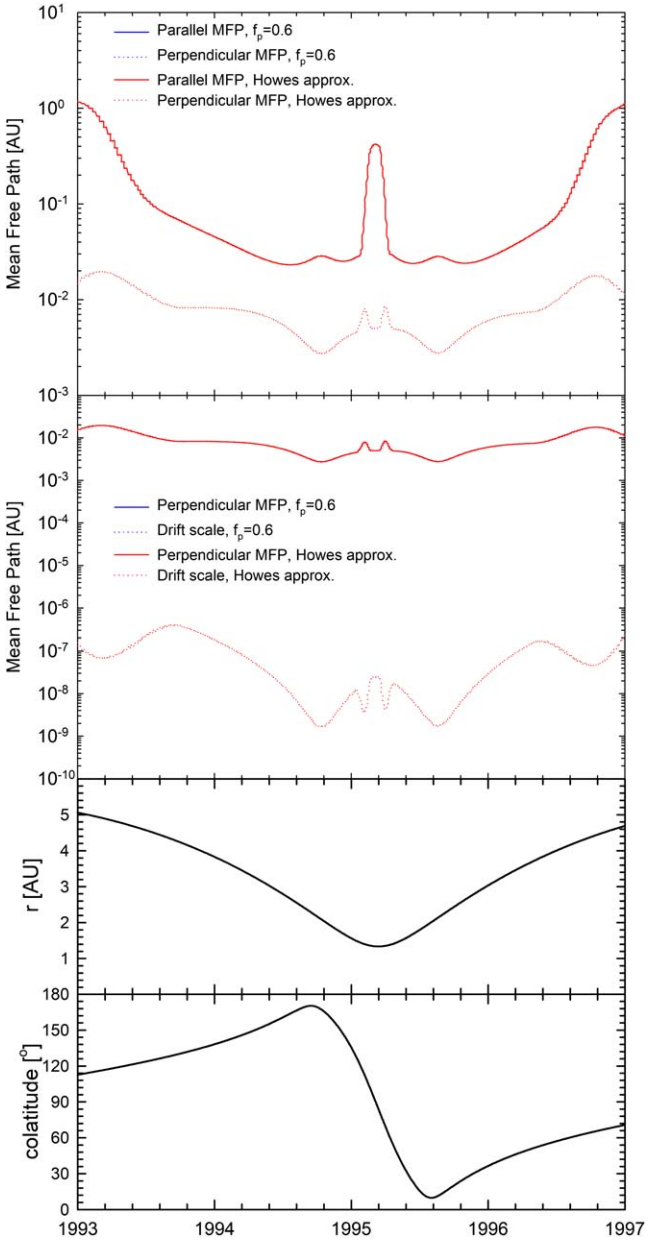


Figure 2. Top panel: 6 MeV parallel and perpendicular MFPs along the trajectory of the Ulysses spacecraft. Middle panel: 6 MeV perpendicular MFP and drift scale along the same trajectory. Bottom panels: radial and colatitudinal trajectory of Ulysses as a function of time.

with the radial distances and colatitudes corresponding to this trajectory shown in the bottom two panels, for a Parker field. In the ecliptic plane, parallel MFPs are considerably larger than perpendicular MFPs, with this difference becoming less prominent at higher latitudes. Perpendicular MFPs display distinct increases at mid-latitudes, reflecting larger 2D variances resulting from increased stream-shear effects due to the transition between the slow and fast solar wind streams as modeled in Equation (8). The influence of the fraction of turbulent energy assumed to heat the protons f_p, as modeled here, does not appear to be significant, as expected from Figure 1. The middle panel of Figure 2 shows a comparison between the perpendicular MFP and the turbulence-reduced drift lengthscale computed from the result presented by N. E. Engelbrecht et al. (2017), and given by

$$\lambda_A = \left[1 + \frac{\lambda_\perp^2}{R_L^2}\frac{\delta B_T^2}{B_0^2}\right]^{-1} R_L, \tag{14}$$

where δB_T^2 denotes the total magnetic variance. This quantity remains between 4 and 6 orders of magnitude smaller than $\lambda_\perp$, due both to the influence of turbulence on drifts as well as the small Larmor radii of 6 MeV electrons. From this result, it can be seen that drift effects would not greatly influence the transport of these particles.

The rigidity, radial, and meridional dependences of the MFPs employed here are further illustrated in Figure 3. The top-left panel of the figure compares the dissipation range onset wavenumber as modeled here (Equation (10)) with extrapolations used in previous studies of the results of R. J. Leamon et al. (2000) in the solar ecliptic plane, as a function of heliocentric radial distance. Significant differences can be seen, particularly at large radial distance. Both the parallel and perpendicular MFPs are essentially rigidity independent at Earth, and remain above the I. D. Palmer (1982) consensus range. This is a result of employing turbulence parameters corresponding to solar minimum conditions: Smaller magnetic variances, for instance, lead to a larger parallel MFP, which in turn, via its $\sim\lambda_\parallel^{1/3}$ dependence, lead to a larger perpendicular MFP. Observational studies (e.g., J. T. Lang et al. 2024), however, report on large variations in these quantities, as indicated by the range of values reported by N. E. Engelbrecht et al. (2022a) in the figure. The bottom-left panel of Figure 3 shows the meridional dependences of the 6 MeV MFPs at 1 au, calculated assuming both the Parker and Schwadron–Parker HMF models. The parallel MFP, similar to what was reported by N. E. Engelbrecht & R. A. Burger (2013b), assumes significantly larger values in the ecliptic than it does at higher latitudes, reflecting the higher turbulence levels in the region dominated by the fast solar wind and in qualitative agreement with the findings of G. Erdős & A. Balogh (2005). Slight dips in the parallel MFP at intermediate latitudes reflect increases in the magnetic variances due to larger stream-shear effects (see also N. E. Engelbrecht & R. A. Burger 2015). For the perpendicular MFP this behavior is reversed, albeit moderately: High-latitude values of this quantity are slightly larger than ecliptic values, with increases at middle latitudes again being due to increased turbulence levels resulting from stream-shear effects. Intriguingly, the minor differences in magnitude between the two HMF models considered here lead to a somewhat smaller parallel MFP at intermediate to higher latitudes when a Schwadron–Parker field is employed, with a correspondingly smaller increase in the perpendicular MFP. The radial dependences of both 6 MeV MFPs in the ecliptic can be seen in the bottom-right panel of Figure 3. Although the same approach is taken here in terms of the TTM model employed as was taken by N. E. Engelbrecht (2019), the parallel MFP used here displays a considerably different radial profile than what is reported in that study, decreasing as a function of radial distance beyond ∼5 au until becoming approximately constant beyond ∼40 au, reflecting the influence of pickup-ion-generated waves on the slab correlation scale. This difference is due to two reasons. First, that study employed a parallel MFP expression derived from the random

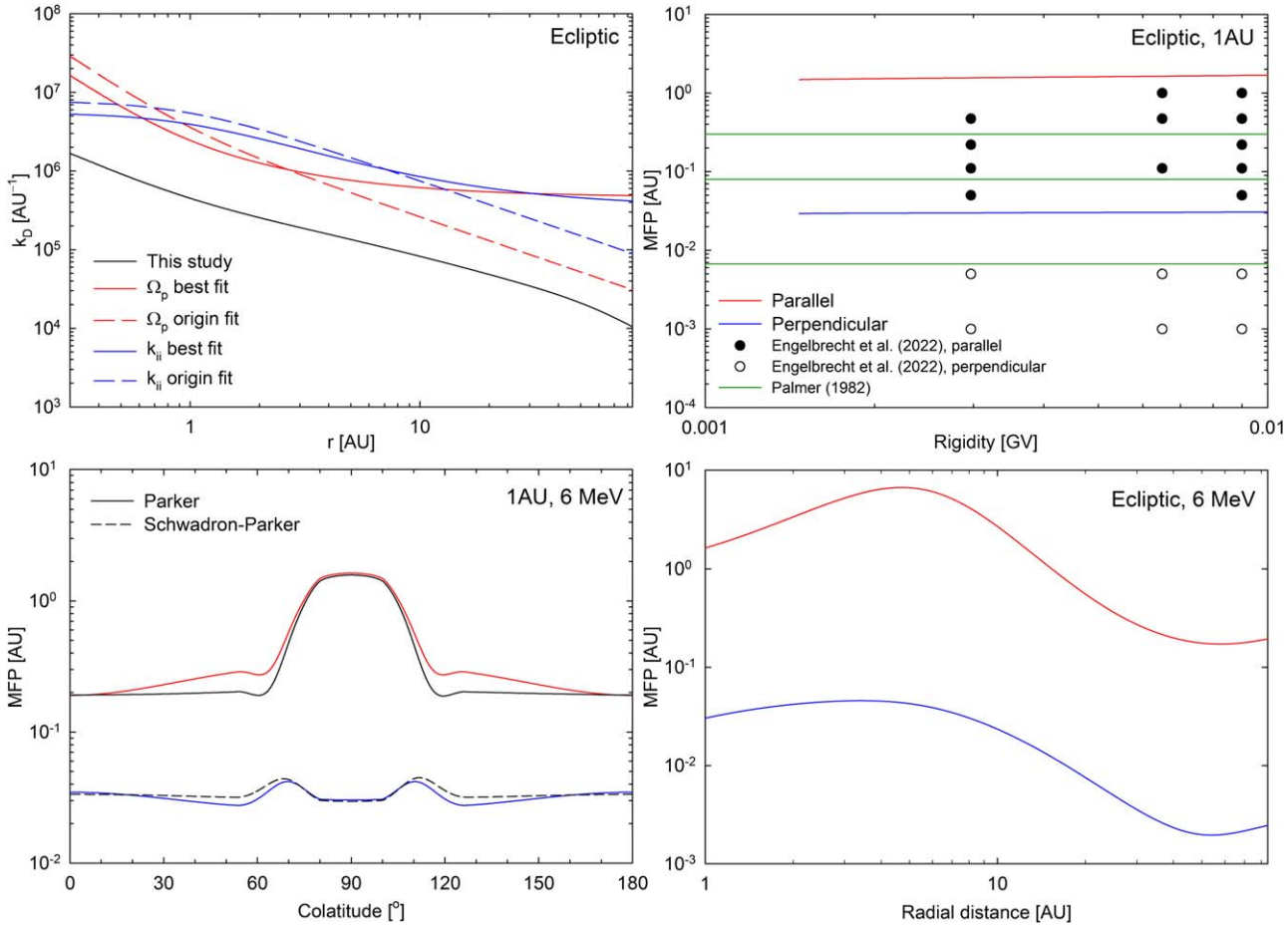


Figure 3. Top-left panel: dissipation range onset wavenumber employed in this study (black line) compared with extrapolations of the same based on the results of R. J. Leamon et al. (2000) used in previous studies as a function of radial distance in the ecliptic plane. Top-right panel: parallel and perpendicular MFPs as a function of rigidity at Earth, alongside the I. D. Palmer (1982) consensus range and values reported by N. E. Engelbrecht et al. (2022a). Bottom-left panel: 6 MeV MFPs as a function of colatitude at 1 au, calculated assuming a Parker as well as a Schwadron–Parker HMF. Bottom-right panel: 6 MeV MFPs as a function of radial distance in the ecliptic, out to 84 au.

sweeping, as opposed to the damping, model of dynamical turbulence. Second, the present study uses a significantly different approach to modeling the onset wavenumber of the dissipation range (see top-left panel of Figure 3). The radial profile of the perpendicular MFP strongly resembles that of $\lambda_{\parallel}$, due to its dependence on that quantity.

3. Model Results

The top panel of Figure 4 shows the modulation model input spectra for GCR electrons (Equation (3)) and Jovian electrons (Equation (2)) as a function of kinetic energy. Below ∼30 MeV the Jovian source produces a higher intensity of electrons than the galactic source, while both sources display a similar energy dependence below ∼10 MeV. The bottom panel of Figure 4 shows the computed galactic and Jovian electron intensities at 1 au, again as a function of kinetic energy, and calculated assuming both a Parker and a Schwadron–Parker HMF, alongside electron observations reported by J. L'heureux & P. Meyer (1976) and D. Moses (1987). Jovian electrons predominate at energies below ∼20 MeV, as expected from previous modulation studies (e.g., S. E. S. Ferreira et al. 2001a; R. R. Nndanganeni & M. S. Potgieter 2018), and fall slightly above observed intensities. This is due to the fact that the observations shown correspond to periods of intermediate to higher solar activity, while the model was run for strictly solar minimum conditions, which would yield larger intensities. GCR electron intensities remain about an order of magnitude smaller than Jovian intensities for the energy range of interest to this study (1−10 MeV), and predominate past ∼40 MeV, where they are significantly larger than the observations. Galactic and Jovian intensities calculated for both HMF models are essentially identical, with the implication that no signal for a Fisk-type field would be expected from an analysis of low-energy electron intensities at Earth. Computed latitude gradients (top panels) and relative amplitudes (middle panels) for GCR electrons alone (left panels) and Jovian electrons alone (right panels) are shown as a function of rigidity in Figure 5 for the Parker HMF (red dashed lines) and the Schwadron–Parker field (blue lines). For galactic electrons, latitude gradients are small and decrease as a function of rigidity, with the use of a Schwadron–Parker field leading to moderately larger latitude gradients than yielded by a Parker field. While this may appear counterintuitive, parallel MFPs at intermediate latitudes are actually moderately smaller than those computed assuming a Parker field (see Figure 3), thereby somewhat inhibiting GCR transport parallel to the HMF. Jovian electron latitude gradients are larger, and negative, due

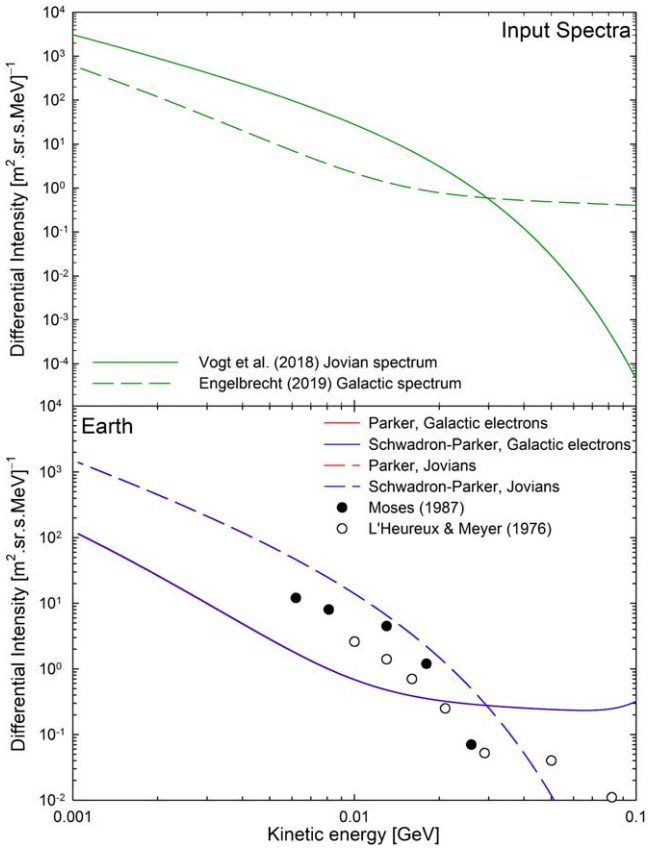


Figure 4. Top panel: input spectra employed in this study, as a function of kinetic energy. Solid line represents the Jovian source spectrum constructed by A. Vogt et al. (2018), and dashed line represents the galactic cosmic-ray electron input spectrum constructed by N. E. Engelbrecht (2019). Bottom panel: Galactic electron and Jovian electron differential intensities at Earth, computed using a Schwadron–Parker hybrid field and a pure Parker field. Electron observations at 1 au, reported by J. L'heureux & P. Meyer (1976) and D. Moses (1987) are also shown, to guide the eye.

to the presence of the Jovian source in the ecliptic plane. Use of a Parker HMF yields no discernable relative amplitudes for GCR electrons, similar to what was reported by K. D. Moloto et al. (2019) for GCR protons, with relatively small relative amplitudes, decreasing as a function of increasing rigidities, result from the use of a Schwadron–Parker field. This decrease qualitatively agrees with the behavior of GCR electron relative amplitudes reported on by N. E. Engelbrecht & R. A. Burger (2010) at higher rigidities, and assuming latitude-independent radial scalings for turbulence quantities, although it should be noted that that study used the somewhat different Fisk–Parker hybrid HMF proposed by R. A. Burger et al. (2008). For Jovians, significant relative amplitudes are seen for a Parker field, again due to the influence of the decentral location of their source. These amplitudes become larger when a Schwadron–Parker HMF is used, reflecting the azimuthal variations in the field geometry. The bottom panels of Figure 5 show the computed relative amplitudes as a function of the latitude gradients. For GCR electrons assuming a Schwadron–Parker HMF, a linear relation reminiscent of that reported by M. Zhang (1997) for protons can be discerned that is not present when a Parker field is assumed, again in qualitative agreement with what was reported by N. E. Engelbrecht & R. A. Burger (2010) at higher rigidities. Any such relationship is masked when Jovian electrons are considered, regardless of HMF model assumed, although the results so computed are clearly different, reflecting the larger relative amplitudes resulting from the use of the Schwadron–Parker field. This is due to the influence of the source location on both the latitude gradients, which are greatly influenced by the presence of the source in the ecliptic plane, as well as on the computed relative amplitudes.

4. Summary and Conclusions

The present study demonstrates that the study of the transport of low-energy electrons, whether of galactic or Jovian origin, can in principle provide valuable, albeit indirect, insights into transport conditions encountered by these particles in the inner heliosphere. These, in turn, can potentially allow for conclusions to be drawn as to the nature of the HMF which cannot necessarily be drawn from direct analyses of existing spacecraft observations of said magnetic field. This is done by investigating the potential influence of a Schwadron–Parker HMF on the transport of both galactic and Jovian electrons, relative to that of the standard Parker field, on intensities computed at Earth and beyond using a 3D, ab initio cosmic-ray modulation model, so as to ascertain what potential signals for the presence of a Fisk-type field would be present in observations of the same. This is of particular interest in the coming years, given the various historical as well as upcoming missions that have (and will) provide a significant amount of electron measurements throughout the inner heliosphere, in particular observations made during the off-ecliptic phase of Solar Orbiter's trajectory (see R. D. Strauss et al. 2024, and references therein), which would allow for the observational investigation of recurrent electron variations at higher latitudes.

As such, the choice of HMF model does not appear to greatly influence GCR and Jovian electron intensities at Earth, and the expectation would be that evidence for such fields would need to be sought elsewhere in the inner heliosphere. For both Jovian and GCR electrons, latitude gradients calculated for both HMF models are not vastly different, with the implication that latitudinal variations in diffusion coefficients due to latitudinal variations in turbulence quantities would play a more significant role. This is similar to what was found by N. E. Engelbrecht & R. A. Burger (2013a), K. D. Moloto et al. (2019), and Z. Shen et al. (2021) for GCR proton modulation. The clearest signal for the presence of a Fisk-type field is expected to come from computed relative amplitudes, which for GCRs are always zero for a Parker field. When a Schwadron–Parker field is assumed, GCR electron relative amplitudes are present, and decrease with increasing rigidity. When Jovians are taken into account, nonzero relative amplitudes are computed for both HMF models, due to the decentral position of the Jovian source. However, relative amplitudes for the Schwadron–Parker field are clearly larger. When only GCR electrons are considered, a linear relationship can be seen between relative amplitudes and latitude gradients, strongly reminiscent of observations presented for protons by M. Zhang (1997). This relationship is masked by the Jovians, but a clear difference between results computed with the Parker and Schwadron–Parker fields can still be ascertained.

Future work will focus on the influence of turbulence-related parameters on Jovian and GCR electron intensities in the inner heliosphere. Potential avenues of refinement for the TTM include improving estimates for the fraction of the turbulent energy that goes toward heating protons, taking into account

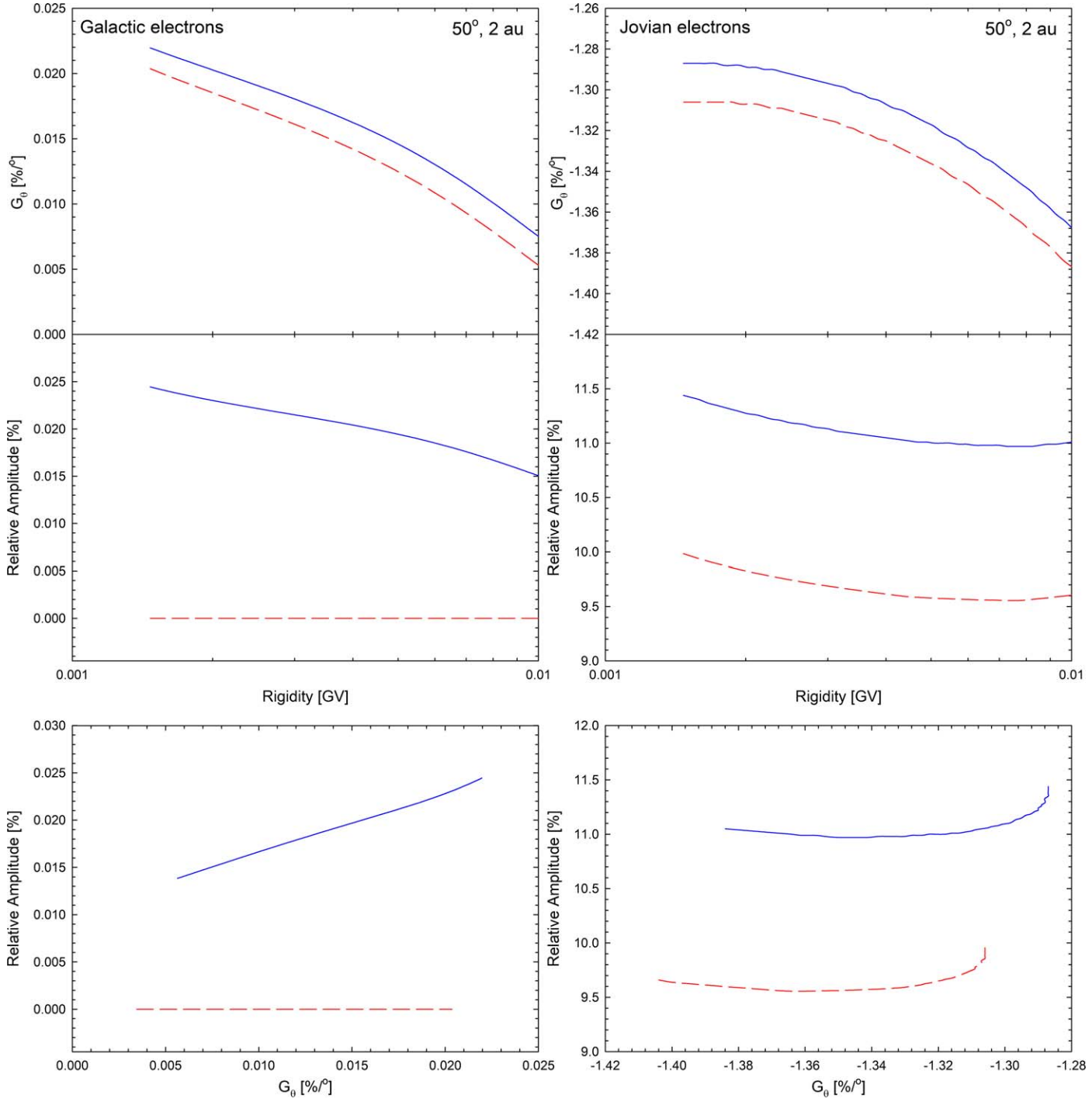


Figure 5. Left panels: Galactic electron latitude gradients and relative amplitudes as a function of rigidity at 2 au and 50° colatitude, as well as the relationship between these quantities, using a Schwadron–Parker hybrid field (blue lines) and a pure Parker field (red dashed lines). Right panels: the same, but for Jovian electrons.

more recent results derived from particle-in-cell simulations of kinetic plasma turbulence (see, e.g., W. H. Matthaeus et al. 2016; S. Roy et al. 2022), turbulence transport modeling (L. Adhikari et al. 2024), and observational analyses (R. Bandyopadhyay et al. 2023), as well as the investigation of the influence of various other TTMs, which are known to yield often considerably different outputs throughout the heliosphere (see, e.g., N. E. Engelbrecht et al. 2022b, and references therein). Solar cycle dependences in both large- and small-scale plasma quantities affecting particle transport will also have to be taken into account, particularly so if detailed comparisons to spacecraft observations have to be made. Lastly, dissipation range turbulence parameters are observed to vary widely (e.g., R. Bruno & V. Carbone 2016), and this variation will need to be taken into account in future modeling endeavors.

Acknowledgments

This work is based on the research supported in part by the National Research Foundation of South Africa (grant No. 137793).

N.E.E. would like to thank P. J. Steyn and A. Vogt for useful discussions on Fisk-type fields and Jovian electron transport.

This research was supported by the International Space Science Institute (ISSI) in Bern, through ISSI International Team project #24-608.

ORCID iDs

N. E. Engelbrecht https://orcid.org/0000-0003-3659-7956

References

Adhikari, L., Zank, G. P., Hunana, P., et al. 2017, ApJ, 841, 85
Adhikari, L., Zank, G. P., Telloni, D., et al. 2024, ApJ, 966, 52
Adhikari, L., Zank, G. P., & Zhao, L. 2021a, Fluid, 6, 368
Adhikari, L., Zank, G. P., Zhao, L. L., Nakanotani, M., & Tasnim, S. 2021b, A&A, 650, A16
Adhikari, L., Zank, G. P., Zhao, L.-L., & Telloni, D. 2022, ApJ, 933, 56
Adriani, O., Barbarino, G. C., Bazilevskaya, G. A., et al. 2011, PhRvL, 106, 201101
Bame, S. J., McComas, D. J., Barraclough, B. L., et al. 1992, A&AS, 92, 237
Bandyopadhyay, R., Meyer, C. M., Matthaeus, W. H., et al. 2023, ApJL, 955, L28
Bavassano, B., Pietropaolo, E., & Bruno, R. 2000a, JGR, 105, 12697
Bavassano, B., Pietropaolo, E., & Bruno, R. 2000b, JGR, 105, 15959
Beck, J. G. 2000, SoPh, 191, 47
Bieber, J. W., Matthaeus, W. H., Smith, C. W., et al. 1994, ApJ, 420, 294
Breech, B., Matthaeus, W. H., Cranmer, S. R., Kasper, J. C., & Oughton, S. 2009, JGRA, 114, A09103
Breech, B., Matthaeus, W. H., Minnie, J., et al. 2008, JGRA, 113, A08105
Bruno, R., & Carbone, V. 2016, Turbulence in the Solar Wind, Vol. 928 (Berlin: Springer)
Burger, R. A. 2005, AdSpR, 35, 636
Burger, R. A., & Hattingh, M. 1995, Ap&SS, 230, 375
Burger, R. A., & Hitge, M. 2004, ApJL, 617, L73
Burger, R. A., Krüger, T. P. J., Hitge, M., & Engelbrecht, N. E. 2008, ApJ, 674, 511
Burger, R. A., & McKee, S. R. 2023, AdSpR, 71, 4916
Burger, R. A., Nel, A. E., & Engelbrecht, N. E. 2022, ApJ, 926, 128
Burger, R. A., Potgieter, M. S., & Heber, B. 2000, JGR, 105, 27447
Burlaga, L. F., & Ness, N. F. 2012, ApJ, 744, 51
Burlaga, L. F., Ness, N. F., Florinski, V., & Heerikhuisen, J. 2014, ApJ, 792, 134
Chen, C. H. K., Bale, S. D., Bonnell, J. W., et al. 2020, ApJS, 246, 53
Chenette, D. L., Conlon, T. F., Pyle, K. R., & Simpson, J. A. 1977, ApJL, 215, L95
Conlon, T. F. 1978, JGR, 83, 541
Cranmer, S. R., Matthaeus, W. H., Breech, B. A., & Kasper, J. C. 2009, ApJ, 702, 1604
Cuesta, M. E., Chhiber, R., Roy, S., et al. 2022, ApJL, 932, L11
Dasso, S., Milano, L. J., Matthaeus, W. H., & Smith, C. W. 2005, ApJL, 635, L181
Davis, N., Chandran, B. D. G., Bowen, T. A., et al. 2023, ApJ, 950, 154
Dempers, N., & Engelbrecht, N. E. 2020, AdSpR, 65, 2072
Dunzlaff, P., Strauss, R. D., & Potgieter, M. S. 2015, CoPhC, 192, 156
Engelbrecht, N. 2012, PhD thesis, North-West Univ.
Engelbrecht, N., & Moloto, K. D. 2021, ApJ, 908, 167
Engelbrecht, N. E. 2017, ApJL, 849, L15
Engelbrecht, N. E. 2019, ApJ, 872, 124
Engelbrecht, N. E., & Burger, R. A. 2010, AdSpR, 45, 1015
Engelbrecht, N. E., & Burger, R. A. 2013a, ApJ, 772, 46
Engelbrecht, N. E., & Burger, R. A. 2013b, ApJ, 779, 158
Engelbrecht, N. E., & Burger, R. A. 2015, ApJ, 814, 152
Engelbrecht, N. E., Effenberger, F., Florinski, V., et al. 2022b, SSRv, 218, 33
Engelbrecht, N. E., & Strauss, R. D. 2018, ApJ, 856, 159
Engelbrecht, N. E., Strauss, R. D., le Roux, J. A., & Burger, R. A. 2017, ApJ, 841, 107
Engelbrecht, N. E., Vogt, A., Herbst, K., Du Toit Strauss, R., & Burger, R. A. 2022a, ApJ, 929, 8
Engelbrecht, N. E., & Wolmarans, C. P. 2020, AdSpR, 66, 2722
Erdős, G., & Balogh, A. 2005, AdSpR, 35, 625
Ferreira, S. E. S. 2005, AdSpR, 35, 586
Ferreira, S. E. S., Potgieter, M. S., Burger, R. A., Heber, B., & Fichtner, H. 2001a, JGR, 106, 24979
Ferreira, S. E. S., Potgieter, M. S., Burger, R. A., et al. 2001b, JGR, 106, 29313
Ferreira, S. E. S., Potgieter, M. S., Heber, B., Fichtner, R., & Kissmann, R. 2003, AdSpR, 32, 669
Fichtner, H., Kleimann, J., Yoon, P. H., et al. 2020, ApJ, 901, 76
Fichtner, H., Potgieter, M., Ferreira, S., & Burger, A. 2000, GeoRL, 27, 1611
Fisk, L. A. 1996, JGR, 101, 15547
Fisk, L. A. 2001, JGR, 106, 15849
Fisk, L. A., & Jokipii, J. R. 1999, SSRv, 89, 115
Fisk, L. A., Zurbuchen, T. H., & Schwadron, N. A. 1999, ApJ, 521, 868
Forsyth, R. J., Balogh, A., & Smith, E. J. 2002, JGRA, 107, 1405
Forsyth, R. J., Horbury, T. S., Balogh, A., & Smith, E. J. 1996, GeoRL, 23, 595
Fraternale, F., Adhikari, L., Fichtner, H., et al. 2022, SSRv, 218, 50
Grasset, O., Dougherty, M. K., Coustenis, A., et al. 2013, P&SS, 78, 1
Halekas, J. S., Whittlesey, P., Larson, D. E., et al. 2020, ApJS, 246, 22
Halekas, J. S., Whittlesey, P. L., Larson, D. E., et al. 2021, A&A, 650, A15
Hattingh, M., Burger, R. A., Potgieter, M. S., & Haasbroek, L. J. 1997, AdSpR, 19, 893
Heber, B. 2013, SSRv, 176, 265
Heber, B., Droege, W., Ferrando, P., et al. 1996, A&A, 316, 538
Heber, B., Gieseler, J., Dunzlaff, P., et al. 2008, ApJ, 689, 1443
Hitge, M., & Burger, R. A. 2010, AdSpR, 45, 18
Horbury, T. S., & Balogh, A. 2001, JGR, 106, 15929
Horbury, T. S., & Osman, K. T. 2008, ISSIR, 8, 55
Howes, G. G. 2010, MNRAS, 409, L104
Isaacs, J. J., Tessein, J. A., & Matthaeus, W. H. 2015, JGRA, 120, 868
Jokipii, J. R. 1966, ApJ, 146, 480
Jokipii, J. R. 2013, SSRv, 176, 115
Jokipii, J. R., Kóta, J., Giacalone, J., Horbury, T. S., & Smith, E. J. 1995, GeoRL, 22, 3385
Kóta, J., & Jokipii, J. R. 1998, SSRv, 83, 137
Kühl, P., Dresing, N., Dunzlaff, P., et al. 2013, CEAB, 37, 643
Lang, J. T., Strauss, R. D., Engelbrecht, N. E., et al. 2024, ApJ, 971, 105
Leamon, R. J., Matthaeus, W. H., Smith, C. W., et al. 2000, ApJ, 537, 1054
L'heureux, J., & Meyer, P. 1976, ApJ, 209, 955
Li, H., Wang, C., & Richardson, J. D. 2008, GeoRL, 35, L19107
Lotz, S., Nel, A. E., Wicks, R. T., et al. 2023, ApJ, 942, 93
Marsch, E., Schwenn, R., Rosenbauer, H., et al. 1982, JGR, 87, 52
Matthaeus, W. H., Dasso, S., Weygand, J. M., et al. 2005, PhRvL, 95, 231101
Matthaeus, W. H., Parashar, T. N., Wan, M., & Wu, P. 2016, ApJL, 827, L7
Matthaeus, W. H., Qin, G., Bieber, J. W., & Zank, G. P. 2003, ApJL, 590, L53
McComas, D. J., Barraclough, B. L., Funsten, H. O., et al. 2000, JGR, 105, 10419
McComas, D. J., Elliott, H. A., Schwadron, N. A., et al. 2003, GeoRL, 30, 1517
McComas, D. J., Rankin, J. S., Schwadron, N. A., & Swaczyna, P. 2019, ApJ, 884, 145
McDonald, F. B., Cline, T. L., & Simnett, G. M. 1972, JGR, 77, 2213
Minnie, J., Bieber, J. W., Matthaeus, W. H., & Burger, R. A. 2007, ApJ, 670, 1149
Moloto, K. D., Engelbrecht, N. E., & Burger, R. A. 2018, ApJ, 859, 107
Moloto, K. D., Engelbrecht, N. E., Strauss, R. D., Moeketsi, D. M., & van den Berg, J. P. 2019, AdSpR, 63, 626
Moraal, H. 2013, SSRv, 176, 299
Moses, D. 1987, ApJ, 313, 471
Müller, D., St, Cyr, O. C., Zouganelis, I., et al. 2020, A&A, 642, A1
Nndanganeni, R. R., & Potgieter, M. S. 2018, Ap&SS, 363, 156
Osman, K. T., & Horbury, T. S. 2007, ApJL, 654, L103
Oughton, S., Dmitruk, P., & Matthaeus, W. H. 2006, PhPl, 13, 042306
Oughton, S., Matthaeus, W. H., Smith, C. W., Breech, B., & Isenberg, P. A. 2011, JGRA, 116, A08105
Paizis, C., Heber, B., Ferrando, P., et al. 1999, JGR, 104, 28241
Palmer, I. D. 1982, RvGSP, 20, 335
Parker, E. N. 1958, ApJ, 128, 664
Parker, E. N. 1965, P&SS, 13, 9
Paternò, L. 2010, Ap&SS, 328, 269
Peaceman, D. W., & Rachford, H. H. 1955, SIAM, 3, 28
Pei, C., Bieber, J. W., Breech, B., et al. 2010, JGRA, 115, A03103
Pilipp, W. G., Muehlhaeuser, K. H., Miggenrieder, H., Rosenbauer, H., & Schwenn, R. 1990, JGR, 95, 6305
Pine, Z. B., Smith, C. W., Hollick, S. J., et al. 2020a, ApJ, 900, 94
Pine, Z. B., Smith, C. W., Hollick, S. J., et al. 2020b, ApJ, 900, 93
Potgieter, M. S. 1996, JGR, 101, 24411
Potgieter, M. S., Haasbroek, L. J., Ferrando, P., & Heber, B. 1997, AdSpR, 19, 917
Pyle, K. R., & Simpson, J. A. 1977, ApJL, 215, L89
Richardson, J. D., Burlaga, L. F., Elliott, H., et al. 2022, SSRv, 218, 35

Roberts, D. A., Giacalone, J., Jokipii, J. R., Goldstein, M. L., & Zepp, T. D. 2007, JGRA, 112, A08103
Roberts, D. A., Goldstein, M. L., Klein, L. W., & Matthaeus, W. H. 1987, JGR, 92, 12023
Rodríguez-Pacheco, J., Wimmer-Schweingruber, R. F., Mason, G. M., et al. 2020, A&A, 642, A7
Roy, S., Bandyopadhyay, R., Yang, Y., et al. 2022, ApJ, 941, 137
Salem, C., Hubert, D., Lacombe, C., et al. 2003, ApJ, 585, 1147
Schwadron, N. A. 2002, GeoRL, 29, 1663
Schwadron, N. A., & McComas, D. J. 2003, GeoRL, 30, 1587
Scime, E. E., Badeau, A. E. J., & Littleton, J. E. 1999, GeoRL, 26, 2129
Scime, E. E., Bame, S. J., Feldman, W. C., et al. 1994, JGR, 99, 23401
Scime, E. E., Littleton, J. E., Gary, S. P., Skoug, R., & Lin, N. 2001, GeoRL, 28, 2169
Shalchi, A., Bieber, J. W., & Matthaeus, W. H. 2004, ApJ, 604, 675
Shen, Z., Qin, G., Zuo, P., Wei, F., & Xu, X. 2021, ApJS, 256, 18
Simpson, J. A., Connell, J. J., Lopate, C., et al. 1995, Sci, 268, 1019
Smith, C. W., Hamilton, K., Vasquez, B. J., & Leamon, R. J. 2006, ApJ, 645, L85
Snodgrass, H. B. 1983, ApJ, 270, 288
Sternal, O., Engelbrecht, N. E., Burger, R. A., et al. 2011, ApJ, 741, 23
Steyn, P. J., & Burger, R. A. 2020, ApJ, 902, 33
Steyn, P. J., Johnson, D., Botha, G. J. J., & Régnier, S. 2024, ApJ, 966, 77
Stone, E. C., Cummings, A. C., McDonald, F. B., et al. 2013, Sci, 341, 150
Strauss, R. D., Dresing, N., Engelbrecht, N. E., et al. 2024, ApJ, 961, 57
Strauss, R. D., & Effenberger, F. 2017, SSRv, 212, 151
Strauss, R. D., Potgieter, M. S., Büsching, I., & Kopp, A. 2011, ApJ, 735, 83
Strauss, R. D., Potgieter, M. S., & Ferreira, S. E. S. 2013, AdSpR, 51, 339
Tautz, R. C., & Shalchi, A. 2012, ApJ, 744, 125
Teegarden, B. J., McDonald, F. B., Trainor, J. H., Webber, W. R., & Roelof, E. C. 1974, JGR, 79, 3615
Teufel, A., & Schlickeiser, R. 2003, A&A, 397, 15
Troskie, J. S., Engelbrecht, N. E., & Steyn, P. J. 2024, ApJ, 970, 144
Usmanov, A. V., Goldstein, M. L., & Matthaeus, W. H. 2016, ApJ, 820, 17
Usmanov, A. V., Matthaeus, W. H., Goldstein, M. L., & Chhiber, R. 2018, ApJ, 865, 25
Vogt, A., Engelbrecht, N. E., Heber, B., Kopp, A., & Herbst, K. 2022, A&A, 657, A39
Vogt, A., Engelbrecht, N. E., Strauss, R. D., et al. 2020, A&A, 642, A170
Vogt, A., Heber, B., Kopp, A., Potgieter, M. S., & Strauss, R. D. 2018, A&A, 613, A28
Webber, W. R., Lal, N., & Heikkila, B. 2017, arXiv:1708.02315
Wenzel, K.-P. 1995, NuPhS, 39, 59
Wenzel, K. P., Marsden, R. G., Page, D. E., & Smith, E. J. 1992, A&AS, 92, 207
Weygand, J. M., Matthaeus, W. H., Dasso, S., & Kivelson, M. G. 2011, JGRA, 116, A08102
Wiengarten, T., Oughton, S., Engelbrecht, N. E., et al. 2016, ApJ, 833, 17
Zank, G. P., Adhikari, L., Hunana, P., et al. 2017, ApJ, 835, 147
Zank, G. P., Dosch, A., Hunana, P., et al. 2012, ApJ, 745, 35
Zank, G. P., Matthaeus, W. H., & Smith, C. W. 1996, JGR, 101, 17 093
Zhang, M. 1997, ApJ, 488, 841
Zhang, M., Qin, G., Rassoul, H., et al. 2007, P&SS, 55, 12
Zhao, L. L., Adhikari, L., Zank, G. P., Hu, Q., & Feng, X. S. 2018, ApJ, 856, 94
Zhao, L. L., Zank, G. P., Adhikari, L., et al. 2020, ApJ, 898, 113
Zhu, X., He, J., Zank, G. P., et al. 2024, ApJ, 966, 88
Zurbuchen, T. H., Schwadron, N. A., & Fisk, L. A. 1997, JGR, 102, 24175